LES OF UNSTEADY VORTEX AERODYNAMICS IN COMPLEX GEOMETRY GAS-TURBINE FUEL INJECTORS

M. Dianat[1], J. J. McGuirk[1], S. Fokeer[1], A.Spencer[1]

[1]Dept. Of Aero. & Auto. Eng., Loughborough University, UK
j.j.mcguirk@lboro.ac.uk

1 Introduction

The challenging NO_x emission targets for civil aeroengine gas-turbines set by ACARE 2020 (2001) (and updated recently in the Flightpath 2050 report) have led to much research over the last decade into the high mass flow, high swirl fuel injector designs that are favoured for so-called 'lean burn' combustors. In contrast to the conventional Rich burn-Quick quench-Lean burn (RQL) technology that has dominated the last several decades (Mosier and Pierce (1980)), lean burn offers the potential of substantially lower NO_x emissions, although there is an increased threat from combustion-induced thermo-acoustic oscillations. A full understanding of the aerodynamic characteristics of gas-turbine fuel injectors (as the baseline for how these might respond to incident acoustic waves) has thus become of great interest for both lean- and rich-burn injectors. Producing an accurate computational approach for predicting the airflow through the multi-swirl passage geometries that have become a fundamental component of gas turbine fuel injectors has therefore attracted appreciable interest.

The fluid mechanics of multi-passage injectors has been shown to be dominated by complex unsteady vortex aerodynamics. Experimental work (Li and Gutmark (2003), Midgley et al. (2005)) has provided detailed evidence of the unsteady dynamics of vortex breakdown including the presence of multiple rotating helical vortex structures and also possibly a precessing vortex core (central recirculation region). The presence of such energetic discrete frequency events embedded within a high intensity turbulent environment raises questions on the optimum approach for numerical prediction. Several authors have compared URANS to LES CFD for gas turbine injector aerodynamics (e.g. Wegner et al. (2004), Dunham et al. (2009). Whilst both LES and URANS CFD approaches were able to capture the gross features of the time-averaged strongly swirling confined flow fairly well, there is an accumulation of evidence which points to satisfactory accuracy only being achieved through LES CFD. Dunham et al. (2009) for example observed that only LES provided spectral analysis in agreement with experiment, capturing the spectral differences over a broad frequency range between test cases with and without a central non-swirling jet. The simulations for the single swirler injector studied indicated that the vortex breakdown process often began inside the injector itself and can lead to negative velocities predicted inside the swirler passages. It is not clear whether this also occurs for more complex multi-swirler geometries. Finally, Cheng et al. (2012) have demonstrated that scalar mixing was also correctly predicted, with all 3 turbulent scalar flux profiles comparing very well between LES and experimental data throughout the primary mixing region, even with a simple SGS model for scalar transport.

Clearly good progress has been made in confirming the suitability of the LES approach for analysis of high swirl injector aerodynamics. However, the previous work still has limitations. The majority of prior work has considered relatively simple (usually single) swirler geometries compared to the complex multi-passage injectors found in practical systems. The need to generate well-resolved LES meshes for complex geometries clearly introduces substantially greater challenge. The present investigation was therefore aimed at focussing attention on an industrially representative multi-passage geometry as a test case for simulation. The flow downstream of injector exit is dominated by turbulent free shear layer processes essentially independent of Reynolds number - implying meshing/resolution and SGS modelling challenges for LES that are fairly straightforward and computationally affordable. If it is necessary for accurate simulation of the unsteady vortex aerodynamics to resolve and model accurately the internal flow in all swirler passages, then the LES challenge may be much more difficult. The present paper describes work carried out (both computational and experimental) to address this important question.

2 Test Case and Experimental Details

2.1 Injector Geometry

Fig. 1 illustrates the fuel injector geometry selected for the simulations presented below. This repre-

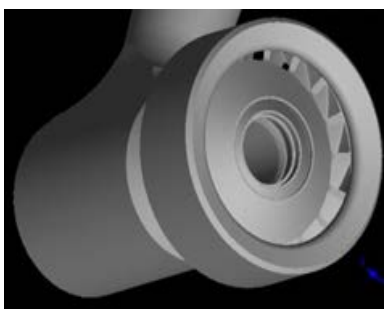

Figure 1: Multi-stream fuel injector geometry

sents a three-stream swirler configuration characteristic of the rich burn injector geometries adopted by the major aeroengine manufacturers for conventional RQL combustor designs. Isothermal (non-reacting) PIV measurements for this injector have been reported by Fokeer and Spencer (2008) and are used here to validate the present LES predictions.

2.2 Test Rig and Measurement Details

Fig.2 illustrates the test set-up - a single isolated injector inserted into an ambient pressure and temperature airflow test rig - also shown in the photograph of Fig.3. Air is drawn into the rig by a downs-

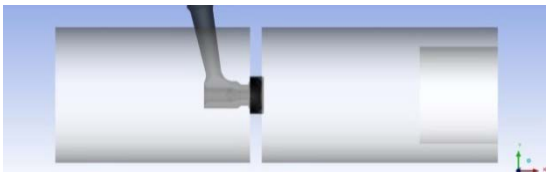

Figure 2: Test set-up (Fokeer and Spencer (2008))

stream centrifugal fan through a smooth bell-mouth intake, followed by a diffuser which dumped into a 1.15m long pipe of 140mm diameter. The injector was mounted centrally in a flange in this pipe with the injector exit plane protruding 2mm from the downstream flange surface. The downstream pipe (also 140mm diameter) contained a central cylindrical blockage of 100mm diameter located 160 mm downstream of the injector exit plane (referred to as x/D_{ref} =0) to leave an annular outlet area. This layout provided a level of confinement and a downstream boundary condition representative of that found in typical full combustor geometries and ensured only positive axial velocities at the working section exit.

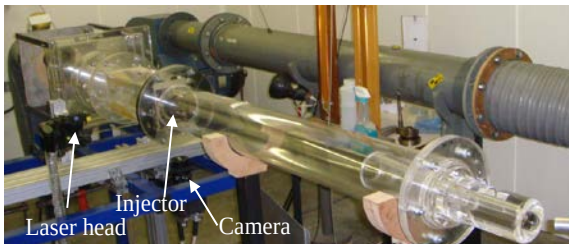

Figure 3: Test facility

The 'burner arm' was left in place and protruded through the inlet pipe wall as seen in Fig.2. The asymmetry this might introduce into the injector feed flow was checked by making measurements on two axial-radial planes downstream of the injector exit, at 0^0 (looking upstream with the burner arm vertical, corresponding to the negative z axis) and 90^0 (corresponding to the positive y-axis); in the 2nd plane the PIV laser light sheet was aligned with the burner arm and in the 1st was rotated by 90^0 relative to the burner arm. Measurements showed that evidence of the burner arm was only present in data taken within the first few mm after the injector exit plane (see Fokeer and Spencer (2008), and Results section); experimental data below are taken from the 90^0 plane.

The pressure drop ($\Delta P/P$) across the injector was set at a level typical of full power engine operation, leading to a Reynolds number (based on reference velocity and length scales characteristic of the bulk velocity U_{ref} and outer diameter D_{ref} at injector exit) of 3.24×10^3. The PIV system used a pulsed laser (twin cavity nano L Litron, wavelength = 532nm, output per pulse 120mJ and interframe time of ~3μs) firing at 4Hz through a combination of spherical and cylindrical lenses to produce a light sheet thickness of ~1mm. The flow tracer was Ondina oil atomized in a TSI 6-jet atomizer producing typically 1-3μm drops. These are known to follow the flow with negligible lag at the velocities employed for the current study, although vortex centres may be devoid of seed particles. The illuminated object plane was recorded using a 4Mpixel digital camera, with a FoV of $35mm^2$ using an interrogation window size of 32^2 pixels, giving a spatial resolution of 0.25mm considering a 50% overlap. The quality of the data may be illustrated by the fact that the number of first choice vectors in any given frame typically exceeded 98%.

Measurements were made in an axial-radial (*x-r*) plane in the immediate vicinity of injector exit, covering a region from r/D_{ref} = 0.1 on one side of the injector centerline to r/D_{ref} = 0.7 on the other side, and from x/D_{ref} = 0.0 (injector exit plane) to 0.8. The slow data capture rate of 4Hz helps ensure that all individual image pairs are statistically independent; 400 frames were used to obtain time-averaged data. To illustrate the flow structure and measurements obtained, Fig. 4 presents non-dimensional axial velocity contours in an axial-radial plane for 0^0 and 90^0 for the region just downstream of the injector exit plane. It

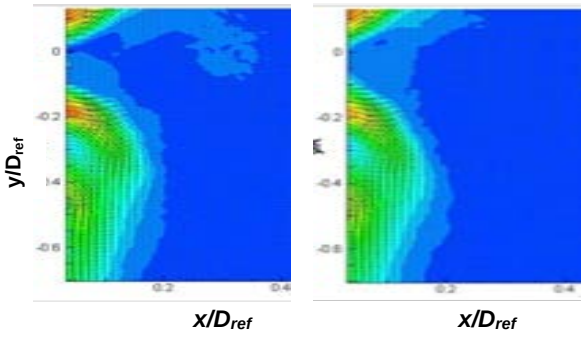

Figure 4: PIV-measured axial velocity contours
Left: 90^0 x-r plane, right: 0^0 x-r plane

is noticeable that the central jet issuing from the injector is quite weak, and does not seem able to penetrate the large central recirculation region to any significant extent. The jets issuing from the inner/outer annular passages (see Fig.1) form distinct swirl cones (particularly the inner). Note also that the very rapid mixing means that the swirling jets diffuse very rapidly, with the outer swirl flow becoming attached to the injector backplate. As a consequence of the rapid mixing, the measurements to be used to validate the LES predictions are taken from the near-field of the injector (x/D_{ref} <0.2).

3 Computational Details

3.1Mathematical formulation and SGS model

The problem considered is the non-reacting and low Mach number aerodynamic behavior of the fuel injector shown in Fig.1. This flow can be considered constant density, so the classical LES filtered governing equations are:

$$\frac{\partial(\overline{u}_i)}{\partial x_i} = 0$$

$$\frac{\partial \overline{u}_i}{\partial t} + \frac{\partial}{\partial x_j}(\overline{u}_i \overline{u}_j) = -\frac{1}{\rho}\frac{\partial(\overline{p} + \tau_{kk}/3)}{\partial x_i} + \frac{\partial \overline{\sigma}_{ij}}{\partial x_j} - \frac{\partial \tau_{ij}}{\partial x_j}$$

$$\overline{\sigma}_{ij} = 2\upsilon \overline{S}_{ij} \qquad \overline{S}_{ij} = \frac{1}{2}\left(\frac{\partial \overline{u}_i}{\partial x_j} + \frac{\partial \overline{u}_j}{\partial x_i}\right)$$

$$\tau_{ij} = (\overline{u_i u_j} - \overline{u}_i \overline{u}_j)$$

Here an overbar represents the filter operation, $\overline{\sigma}_{ij}$ is the resolved viscous stress tensor defined in terms of the molecular kinematic viscosity υ and $\overline{S}_{ij}$ the filtered (resolved) strain rate tensor, and τ_{ij} is the unknown residual/SGS stress tensor.

The eddy viscosity SGS model suggested by Vreman (2004) has been used. This model was chosen because of the robust properties of an eddy viscosity model for flows requiring complex mesh structure, and the evidence reported by Vreman that, unlike the standard Smagorinsky model, its dissipation is small in transitional and near-wall regions, and the model performed as well as the dynamic Smagorinsky model in both turbulent channel flow and transitional mixing layer test problems (but at 50% less computational cost). The model replaces τ_{ij} by the following relations:

$$\tau_{ij} = -2\upsilon_{sgs}\overline{S}_{ij} + \tau_{kk}\frac{\delta_{ij}}{3}$$

$$\upsilon_{sgs} = c\sqrt{\frac{B_\beta}{\alpha_{ij}\alpha_{ij}}} \qquad \alpha_{ij} = \frac{\partial \overline{u}_j}{\partial x_i} \qquad \beta_{ij} = \Delta_m^2 \alpha_{mi}\alpha_{mj}$$

$$B_\beta = \beta_{11}\beta_{22} - \beta_{12}^2 + \beta_{11}\beta_{33} - \beta_{13}^2 + \beta_{22}\beta_{33} - \beta_{23}^2$$

Δ_m is the filter width in direction m (in the simulations Δ_m was assumed the same in all directions and equal to the cube root of the local cell volume). The model constant c is related to the Smagorinsky constant C_S by $c \sim 2.5C_S^2$ and a value for $C_S = 0.17$ was used in the simulations reported below.

3.2 LES code and numerical details.

The simulations were performed using the Rolls-Royce CFD code PRECISE-UNS, which is described in detail in Anand et al. (2013). This is a low Mach number, face-based, co-located, implicit, finite-volume code, which uses hybrid unstructured (hexahedral/tetrahedral) meshes. The pressure-correction equation is solved using a version of the SIMPLE algorithm. The origin of the code is in the open source code Dolfyn (2001), and the baseline approach to numerical discretisation is as described in Ferziger and Peric (2002). Both spatial and temporal discretisation are implemented by a (stability promoting) deferred correction approach with a weighted blending of 1st and 2nd order accurate schemes; for the LES predictions of relevance here, pure 2nd order schemes were used. The code has been well validated against standard RANS and LES test problems and complex industrial combustor flows (Anand et al. (2013)).

3.3 LES mesh design strategy.

The complexity of the injector internal geometry, the use of an unstructured mesh, and the requirement to resolve both free shear flows outside and near-wall flows inside the injector demand a well-planned strategy for LES mesh design. A description of the approach adopted is given here and illustrated pictorially in Fig. 5.

The conventional RANS CFD strategy of continued mesh refinement to establish numerical accuracy of predictions is not readily transferable to LES CFD. Further, it is well known that for LES, the mesh quality is as important as the mesh density. For example, Vanella et al. (2008) have shown that a sudden coarsening of the mesh can be very damaging for LES, since this causes an energy "pile-up" at the smallest resolved scale in the coarser mesh region. There have thus been several studies, for example by Celik et al. (2005) or Gant (2010), to explore the development of mesh quality assessment measures for LES or to explore the application of these techniques to flows of industrial complexity. It is clear that an optimum strategy for LES mesh design should be based on these best practice guidelines for a "well-resolved" mesh in the context of LES.

Different guidelines have necessarily to be used depending on whether the local flow is expected to be wall-dominated or free shear dominated. For high Reynolds number flow, Pope (2000) suggested that >80% of the local fluctuating energy should be captured by the LES mesh if this is to be considered well-resolved (the same criterion was used in Celik et al. (2005)). For near-wall flows, Piomelli and Balaras (2002) have recommended that for wall-dominated turbulence, an adequate mesh must meet maximum cell size criteria. Since the size of near-wall turbulent eddies scales in (Reynolds number dependent) viscous wall units, they recommended $\Delta x^+ < 100$, $\Delta y^+ < 1$ and $\Delta z^+ < 20$, for well-resolved simulations in near wall flows (x, y, z are streamwise, wall normal and wall parallel directions).

The strategy adopted for the present problem has been firstly to design and check that the mesh in free-shear layer dominated regions is well resolved (e.g. the region just downstream of injector exit as seen in Fig.4), and then to address important near wall regions. A mesh-related criterion for greater than 80%

fluctuating energy to be captured in the resolved scales may be estimated by considering two expressions for the turbulence energy dissipation rate ε, the first using an approximation for the integral length scale of turbulence (l_t) as obtained from k_t and ε, and the second using the SGS model-based estimation of ε suggested by Moeng and Wyngaard (1988), thus:

$$l_t = \frac{k_t^{3/2}}{\varepsilon}, \quad \varepsilon = C_\varepsilon \frac{k_{sgs}^{3/2}}{\Delta}, \quad k_t = k_{res} + k_{sgs}$$

Where k_t, k_{res}, and k_{sgs} represent estimates for total, resolved and SGS turbulence energy respectively.

The above relations may be manipulated to give the following constraint on the mesh to match the 80% resolution requirement (using $C_\varepsilon = 0.93$ (Moeng and Wyngaard (1988)):

$$\frac{l_t}{\Delta} > \left[\frac{1}{0.2C_\varepsilon^{2/3}}\right]^{3/2} \quad i.e. \quad \frac{l_t}{\Delta} > 12 \quad for \quad \frac{k_{res}}{k_t} > 0.8$$

Finally, by making an equilibrium approximation at the SGS scale, an estimate for k_{sgs} may be derived and hence k_{sgs}/k_t estimated:

$$k_{sgs} = 0.099\Delta^2 S^2 \quad where: \quad S = (2\bar{S}_{ij}\bar{S}_{ij})^{1/2}$$

A three step approach to using this concept was thus applied as follows:

(i) An initial mesh, referred to in Fig. 5 as 'coarse' - 1.2 million cells with 34,000 inside the injector - was chosen based on standard practice for RANS CFD (fine mesh in expected high gradient regions) and a k-ε solution obtained; an estimate of local turbulence integral scale $l_t = k^{3/2}/\varepsilon$ was extracted and examined with respect to the local mesh size Δ.

(ii) Based on the values of l_t/Δ observed on the coarse mesh, this was modified into a 'medium' mesh to satisfy $l_t/\Delta > 12$ – 7.2 million cells with 340,000 inside the injector - and a first LES solution obtained.

(iii) The ratio of k_{sgs}/k_t from the medium mesh LES solution was examined, and the mesh further modified to satisfy $k_{sgs}/k_t < 0.2$ where necessary; this is referred to in Fig.5 as 'fine mesh away from walls' - 12.2 million cells and 411,000 inside the injector.

Examination of unsteady features and statistics from the medium and fine meshes (see Results section below) showed a relatively small difference. The medium mesh was therefore finally refined inside the injector following the guidelines of Piomelli and Balaras (2002) for a wall-resolving LES mesh. On examination of predictions from the medium/fine mesh solutions, it was observed that the main origin of large scale unsteadiness was in the central (pilot) swirler. Thus, in the first instance, the near wall refinement was concentrated on the central swirler passage walls and vanes. This resulted in a final overall mesh size of 12.4 million cells with 1.1 million inside the injector.

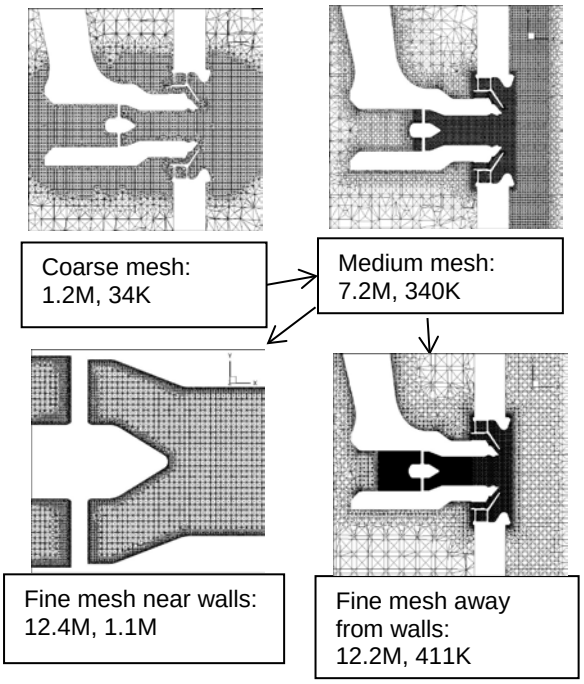

Figure 5: LES mesh design strategy

It is worth commenting finally that the ultimate check of LES mesh quality would have been to extract the integral length scale l_t (from, say the axial velocity field) via evaluation of 2-point spatial velocity correlations, and repeat the $l_t/\Delta>12$ check. This is certainly possible from an LES solution, although computationally expensive. This was not attempted in the present work, but may be worthwhile to check whether use of l_t from a k-ε solution is adequate.

4 Results and Discussion

Fig. 6 presents an overall view of predicted time-averaged axial velocity contours on the z=0 plane (NB in what follows all velocity and length variables are non-dimensionalised using U_{ref} and D_{ref} respectively). Note that the velocity magnitudes inside and outside the injector differ markedly, so two views are shown, one (Fig. 6 (top)) with contour levels emphasising the internal injector flow, and the second (Fig. 6 (bottom)) with levels chosen to emphasise the downstream flow. Inside the injector peak velocities reach greater than $5U_{ref}$ and clear evidence of the rotating wakes created by the central (pilot) swirler can be seen (close up views shown below). There is evidence of a thin recirculation region on the injector centreline throughout the internal injector passage and downstream of the central bullet, producing a peak predicted negative velocity of about $-1U_{ref}$ just inside the injector exit plane. The downstream recirculation has much larger regions of around $-0.5U_{ref}$

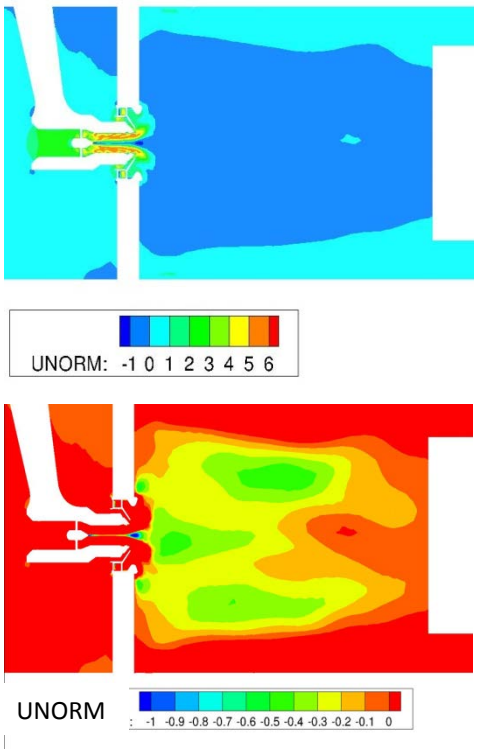

Figure 6: Predicted axial mean velocity, z=0 plane; top-inside injector, bottom - recirculating region

and a structure which shows a recirculation zone near the injector exit with peak velocity on the centreline, and a toroidal zone further downstream where peak negative velocities are off-centre.

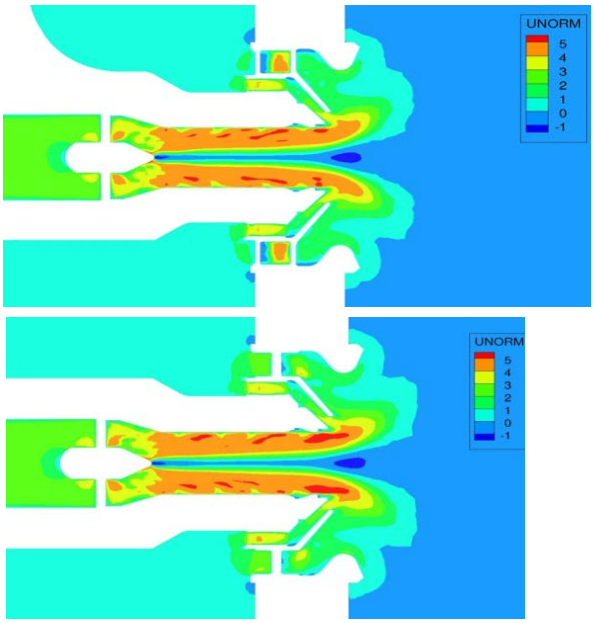

Figure 7:Predicted axial mean velocity, injector flow top: z = 0 plane, bottom: y =0 plane

Fig.7 presents a zoomed-in view to illustrate the injector internal flow structure on the z=0 plane (top) and y=0 plane (bottom). This allows the small differences cause by the presence of the burner arm to be identified. The streaks representing high axial velocity regions show the central swirler passage flows as these rotate around the injector centreline; comparison of these between the views shown indicate the effect of the burner arm blockage of the injector entry flow. Only the highest velocity regions are affected, even one contour level lower the flow is close to axisymmetric, and this is also true in the flow outside the injector exit plane. The low velocity zones near the passage walls where the swirler vane wake fluid accumulates are similar between the two views.

Fig. 8(i) allows a comparison of the increased mesh resolution between the medium and fine meshes described above. In particular the grids on two axial planes are shown; the first intersects the central swirler and the second cuts the inner/outer swirlers. Only part of the swirlers is shown to allow a zoomed-in view of the mesh around the vanes and in the swirler passages. To examine the different flow structures brought about by this mesh refinement, Fig. 8(ii) presents predicted iso-surfaces of the Q criterion as conventionally used to identify vortex structures in the flow (the fluctuating velocity field is here used to evaluate Q):

$$Q = -\frac{1}{2}\frac{\partial \overline{u}_i}{\partial x_j}\frac{\partial \overline{u}_j}{\partial x_i}$$

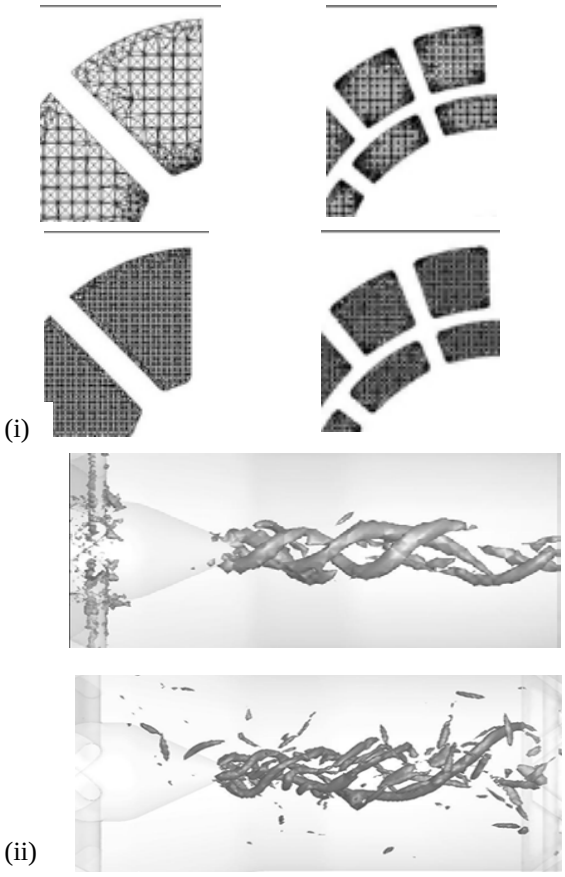

Figure 8: (i) medium/fine mesh comparison; (ii) medium/fine mesh solutions – instantaneous snapshots of central swirler vortex

These images show that both meshes predict a double helical vortex structure in the internal injector unsteady velocity field, very similar to that noted in previous measurements and LES CFD studies of simpler fuel injector geometries (Midgley et al. (2005) and Dunham et al (2009)). The images also confirm that, as in the simple injector geometry of Midgley et al. (2005), the vortex breakdown process also begins inside the injector in geometries typical of industry practice.

Differences between the two solutions are seen, with the finer mesh showing a finer scale structure, but the predicted double vortex structure remained, and examination of 1st and 2nd moment velocity statistics between the two meshes and comparison with measured data outside the injector (see below) produced very similar results. These observations - that (i) the primary driver of the unsteady flow has its origin in the central swirler (more evidence of this given below), and (ii) the medium/fine meshes showed similar statistics, was the reason the final level of grid refinement for near wall zones was restricted to the central swirler region as described above.

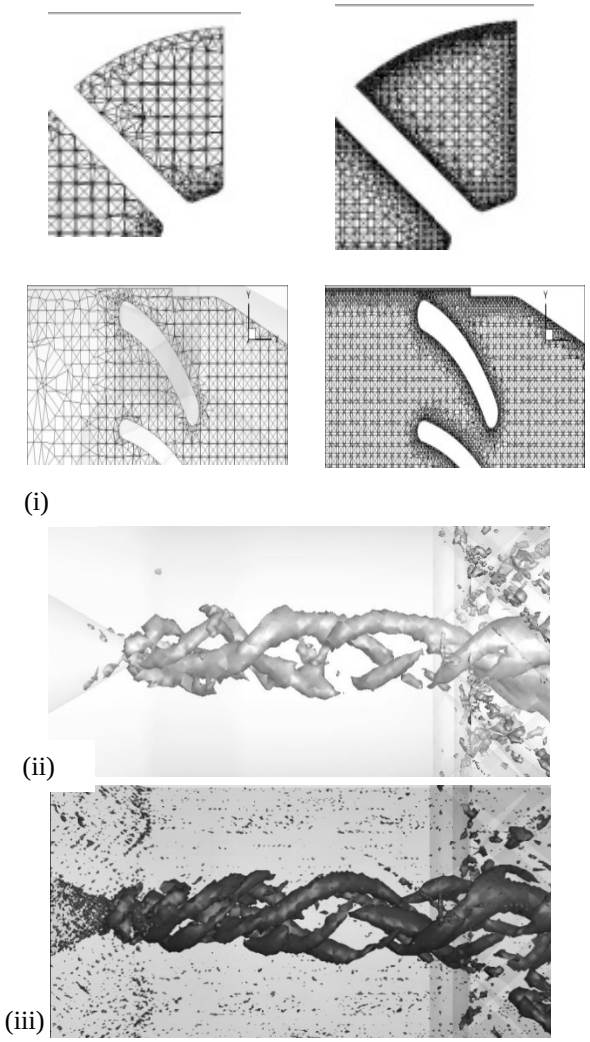

Figure 9:(i) medium/wall refined mesh comparison; helical vortex structure comparison: (ii) medium and (iii) wall refined meshes

Fig. 9 (i) illustrates the wall refined mesh designed, indicating in particular the extra resolution included in the vicinity of central swirler vane walls. Fig. 9 (ii) and (iii) again use iso-surfaces of Q to show the change in the double helical vortex structure brought about by the extra wall refinement – only relatively little change has been produced.

If the level of the Q iso-surface is altered to capture the swirler vane vortex structures as well as the central helical structures, then Fig.10 shows that the extra wall refinement has enabled the vane wakes to be resolved better, allowing improved capture of their propagation down the injector passage. Once again, as shown below, this does have an effect on the injector exit flow velocity statistics; this is small but quite noticeable.

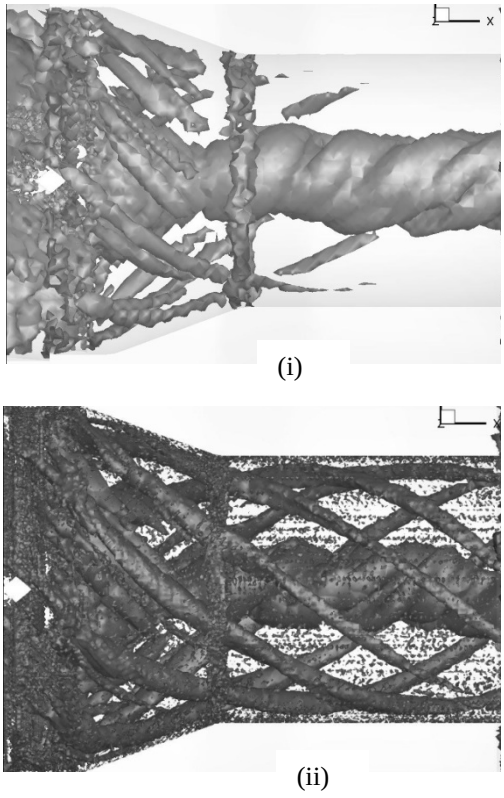

Figure 10:central swirler vane vortex comparison (i) medium and (ii) wall refined meshes

It is clearly of interest to examine what happens when the helical vortex structure emerges from the injector exit. This is shown in Fig. 11 where it is seen that the predicted behaviour is of a rotating helical structure which wraps itself around the large central recirculation zones described in Fig. 6. This is visualised much better in a video, which also shows that the 'wind' angle of the vortex is opposite in direction to the main swirl velocity component, as expected from the most unstable mode of a swirling jet. This relationship between helical vortex wind angle and bulk swirl direction may be seen best in Fig. 12.

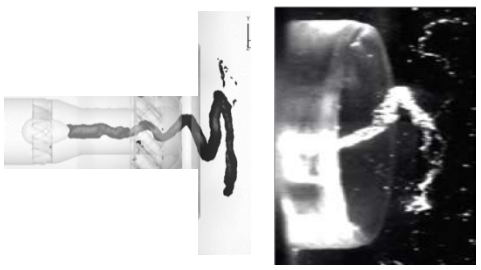

Figure 11 Unsteady rotating vortex structure

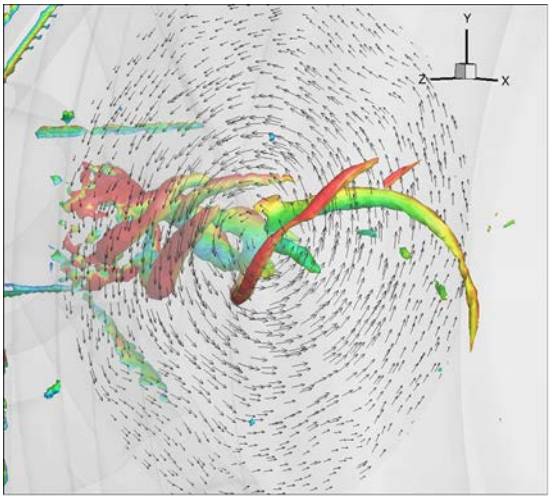

Figure 12: Illustration of relationship between vortex helix angle and bulk swirl direction.

The correctness of the LES-predicted unsteady vortex behaviour was confirmed in a water flow test using the same injector. In this test, the low pressure zone in the centre of the vortex caused cavitation and enabled the behaviour of the vortex to be clearly visualised, as seen on the right in Fig.11.

Resolution of the vane wakes is also important if the turbulence energy created by the injector swirlers and feeding into the injector exit flow is to be properly captured - an illustration of this is given in Fig. 13. This shows the predicted turbulence energy contours just downstream of the central swirler exit, and also on the z = 0 plane. The peak turbulence energy is found to be closely aligned with the vane trailing edge, and this subsequently accumulates near the injector passage outer wall and is convected by the bulk swirl in a helical path towards injector exit where it feeds into the recirculation zone.

Finally, quantitative comparison with PIV airflow experiments for the flow downstream of the injector is shown in Fig.14. The comparison focusses particular attention on the high shear regions immediately outside the injector exit plane - profiles are presented at x/D_{ref} = 0.034, 0.087, 0.14. There is some improvement with mesh refinement to resolve

(i)

(ii)

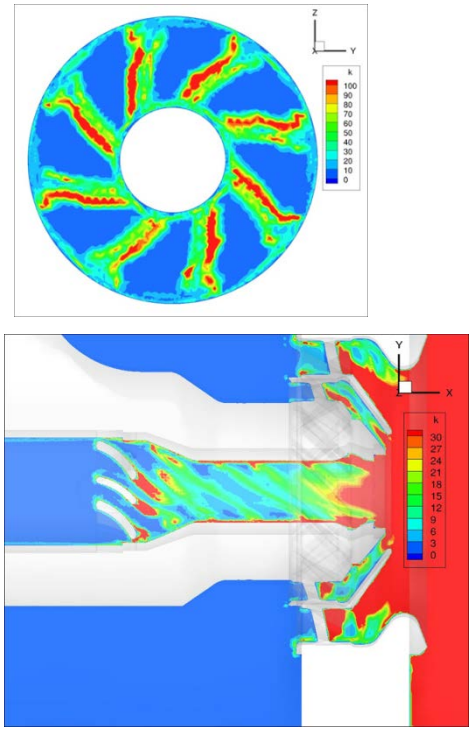

Figure 13:Predicted k contours at: (i) x/D_{ref} = -0.76, (ii) z/D_{ref} = 0

vane wakes, particularly for the axial velocity where the peak negative values in all three profiles are better predicted after the vane wake resolution was improved. The mean transverse velocity results are less affected by the vane wakes. Both axial and radial turbulent intensities are well captured; the double peaks in the axial component and its radial location indicate that the positions of the swirl cone shear layers are well predicted. The intensities decay somewhat faster downstream than in the measured results.

5 Summary and Conclusions

The work described in this paper investigated a novel procedure for LES mesh design for complex geometry flows. This was successfully applied to a gas-turbine fuel injector geometry representative of current industrial practice. Careful mesh design enabled confidence to be built that the LES methodology resolved all important geometry and flow features adequately. The flow in this complex geometry was observed to behave as in earlier studies on much simpler (single swirler) geometries, in particular vortex breakdown again occurred inside the injector, and was well predicted by LES. The use of a fine near wall mesh for the swirler vanes was observed to influence the near injector discharge flow, and required an appropriate choice of SGS model with low dissipation in regions of low turbulence Reynolds number. Experimental validation of the accuracy of the LES predictions for internal and external injector aerodynamics was achieved using PIV measurements carried out on an identical injector geometry.

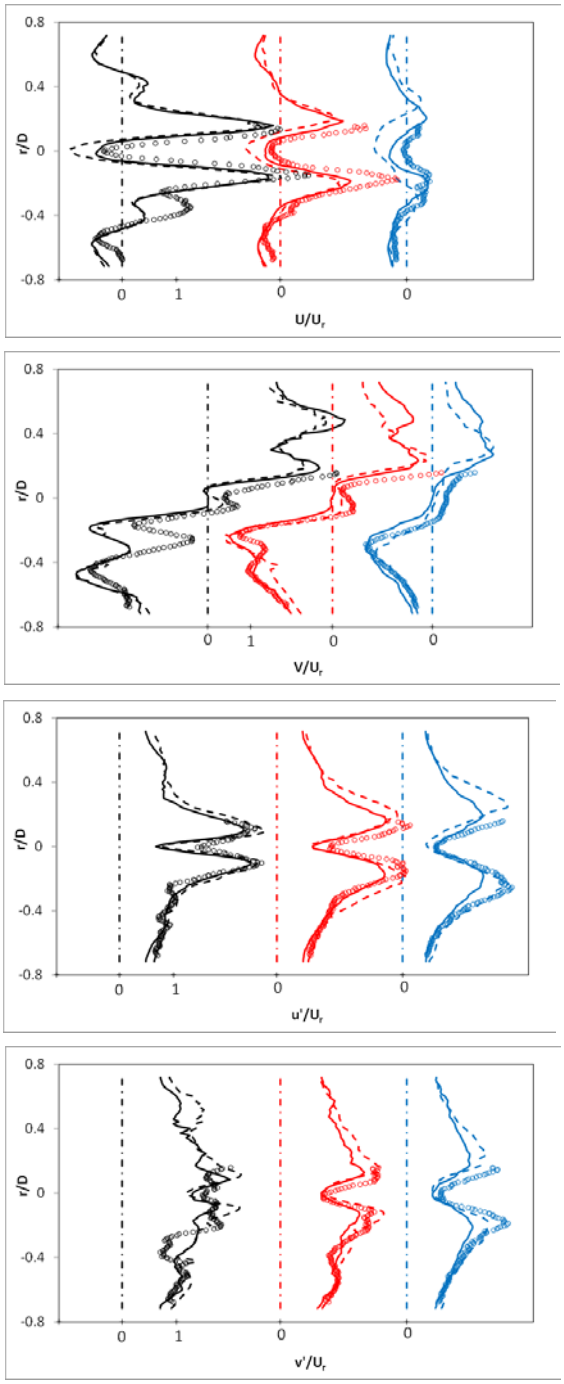

Figure 14:Axial and transverse velocity statistics: non- dimensional mean (U, V) & rms (u', v') solid –wall refined mesh, dashed – medium mesh, symbols – PIV

Acknowledgements

The computational work reported here was funded by EPSRC as part of the SAMULET project, Grant No. EP/G035229/1.

References

ACARE 2020 (2001) European Aeronautics - A Vision for 2020: Report of the EU Group of Personalities, ISBN 92-894-0559-7.

Anand, M. S., Eggels, R., Staufer, M., Zedda, M., Zhu, J. (2013) An Advanced Unstructured Grid Finite Volume Design System For Gas Turbine Combustion Analysis: ASME Paper GTINDIA2013-3537.

Celik, I. B., Cehreli, Z. N., Yavuz, I. (2005) Index of resolution quality for Large Eddy Simulations, *ASME Jnl. of Fluids Eng.*, Vol. 127, pp 949-958.

Cheng, L., Dianat, M., Spencer, A., McGuirk, J. J. (2012) Validation of LES Predictions of Scalar Mixing in High-swirl Fuel Injector Flows: *Flow Turbulence and Combustion*, Vol. 88, pp 146-168.

Dolfyn (2001) www.dolfyn.net.

Dunham, D., Spencer, A., McGuirk J. J., Dianat, M. (2009) Comparison of Unsteady Reynolds Averaged Navier Stokes and Large Eddy Simulation CFD Methodologies for Air Swirl Fuel Injectors: *ASME Jnl. of Eng. for GT & Power*, Vol. 131, pp 011502.

Ferziger, J. H. and Peric, M. (1996) *Computational methods for Fluid Dynamics*, Springer, Berlin.

Fokeer, S. and Spencer, A. (2008) PIV Measurements for Trent Rich Burn Fuel Injectors: Dept. of Aero. & Auto. Eng. Internal Report TT08R03.

Gant, S. E. (2010) Reliability issues of LES-related approaches in an industrial context, *Flow Turbulence and Combustion*, Vol. 84, pp 325-335.

Li, G. and Gutmark, E.J. (2003) Geometry Effects on the Flowfield and Spectral Characteristics of a Triple Annular Swirler: ASME Paper GT2003-38799.

Midgley, K., Spencer, A., McGuirk, J.J. (2005) Unsteady Flow Structures in Radial Swirl Fed Fuel Injectors: *J. of Eng. for GT & P.* Vol. 127, pp 755-764.

Moeng, C-H and Wyngaard, J. C. (1988) Spectral analysis of LES models of the convective boundary layer: *Jnl. Of the Atmos. Sci.*, Vol. 45, pp3573-3587.

Mosier, S. A. and Pierce, R. M. (1980) Advanced combustion systems for stationary gas turbine engines: Vol. 1 – review and preliminary evaluation: US EPA Report No. EPA-600/7-80-0171.

Piomelli, U. and Balaras, (2002) Wall-layer models for Large Eddy Simulations: *Annual Review of Fluid Mechanics*, Vol. 34, pp. 349-374.

Pope, S. B. (2000) Turbulent Flows: *Cambridge University Press.*

Vanella, M., Piomelli, U., Balaras, E. (2008) Effect of grid discontinuities on Large Eddy Simulation statistics and flow fields, *Jnl. of Turb.*, Vol. 9 pp 1-23.

Vreman, A. W. (2004) An Eddy-viscosity SGS Model for Turbulent Shear Flow: Algebraic Theory and Applications: *Phys of Fluids*, Vol. 16, pp. 3670-3681.

Wegner, B., Maltsev, A., Schneider, C., Sadiki, A., Dreizler, A., Janicka, J. (2004) Assessment of Unsteady URANS in Predicting Swirl Flow Instability Based on LES and Experiments*: Int. J. of Heat and Fluid Flow*, Vol.25, pp. 528–535.